

Article

# Rodlike $\text{YMn}_2\text{O}_5$ Powders Derived from Hydrothermal Process Using Oxygen as Oxidant

Jun Shi <sup>1</sup> , Jing Wang <sup>1,\*</sup>, Huifen He <sup>1</sup>, Yang Lu <sup>1,2</sup> and Zhongxiang Shi <sup>1</sup>

<sup>1</sup> Liaoning Key Laboratory for Fabrication and Application of Superfine Inorganic Powders, Dalian Jiaotong University, Dalian 110621, China; shijun@djtu.edu.cn (J.S.); hehuifen163@163.com (H.H.); luyang4967@126.com (Y.L.); szx492670794@163.com (Z.S.)

<sup>2</sup> Department of Materials Science and Engineering, Yingkou Institute of Technology, Yingkou 115014, China

\* Correspondence: wangjing@djtu.edu.cn; Tel.: +86-0411-8410-9776

Received: 7 January 2020; Accepted: 6 February 2020; Published: 10 February 2020



**Abstract:** A facile approach is proposed herein to fabricate  $\text{YMn}_2\text{O}_5$  powders with the hydrothermal method with oxygen as an oxidant. The structure and morphology of the as-synthesized  $\text{YMn}_2\text{O}_5$  powders were characterized by XRD, SEM, and high-resolution transmission electron microscopy (HRTEM). The results manifested that the main factors that affected the formation of the rod-like  $\text{YMn}_2\text{O}_5$  structures were the stirring time, hydrothermal temperature, and hydrothermal time. The oxidation time in the air had a remarkable effect on the final product by oxidizing  $\text{Mn}^{2+}$  ions to  $\text{Mn}^{3+}$  ions and  $\text{Mn}^{4+}$  ions. The obtained  $\text{YMn}_2\text{O}_5$  powder was single crystalline and possessed a nanorod morphology, where the growth direction was along the c axis. The possible formation mechanism involved a dissolution–crystallization mechanism. Under the 397 nm excitation, the  $\text{Mn}^{4+}$  ions exhibited an intense orange emission at 596 nm. The energy bandgap of  $\text{YMn}_2\text{O}_5$  powders was 1.18 eV.

**Keywords:** yttrium manganite; hydrothermal method; formation mechanism; luminescent properties

## 1. Introduction

Multiferroic materials, which are a kind of multifunctional material with two or more kinds of ferroelectric and ferromagnetic properties, have been widely applied in the fields of material science and condensed matter physics [1–4]. In recent years, this kind of material has attracted extensive attention and resulted in the development of new magnetoelectric devices, spin electronic devices, and high-performance information storage.

Common perovskite manganese compounds with orthogonal structures are a kind of multiferroic material, such as  $\text{TbMnO}_3$ ,  $\text{DyMnO}_3$ , and  $\text{TbMn}_2\text{O}_5$  [5–10]. The conventional approaches to the preparation of perovskite manganese compounds include the solid-state method [11], sol-gel method [12,13], polyacrylamide gel method [14–17], spark plasma sintering method [18], electrospinning method [19], and hydrothermal method [20,21]. The sol-gel method and the spark plasma sintering method require high-temperature calcination in the intermediate and final stages of synthesis, which may cause product agglomeration and make it difficult to control the reaction. Although the synthesis temperature required for the polymer gel method is high, the purity of the product is low. By comparison, the hydrothermal method is able to control particle size, morphology, and phase and is the most common method for preparing multivalent manganese oxides [20,21]. Therefore, the preparation of nanopowder materials by this method has broad development possibilities.  $\text{Mn}^{4+}$  ions are usually found on octahedral sites of solids. They exhibit both broadband excitation and sharp emission lines due to the distinct electronic structure [22]. However, the luminescent properties of  $\text{YMn}_2\text{O}_5$  have hardly been reported.

Many pieces of the literature have reported the effect of pH on the morphology of  $\text{YMn}_2\text{O}_5$  powder, and it has been found that nanorod-like powders can be obtained at low pH [21]. In this

paper, the effects of air oxidation and hydrothermal conditions on the formation of  $\text{YMn}_2\text{O}_5$  powder were studied, and the formation mechanism of the powder was also discussed. At the same time, the luminescent properties of  $\text{YMn}_2\text{O}_5$  powder were investigated.

## 2. Materials and Methods

### 2.1. Materials Synthesis

The raw materials included yttrium nitrate hexahydrate ( $\text{Y}(\text{NO}_3)_3 \cdot 6\text{H}_2\text{O}$ , Energy Chemical, Shanghai, China), manganese chloride tetrahydrate ( $\text{MnCl}_2 \cdot 4\text{H}_2\text{O}$ , DaMao Chemical Reagent Factory, Tianjin, China), and potassium hydroxide (KOH, DaMao Chemical Reagent Factory, Tianjin, China). All chemicals were analytical grade and used without further purification. Certain amounts of  $\text{MnCl}_2$  and  $\text{Y}(\text{NO}_3)_3$  were used to prepare 0.2 and 0.4 mol/L solutions. First, a 4 mmol  $\text{MnCl}_2$  solution and a 9 mmol KOH solution were added to deionized water and stirred in the air at room temperature for different times (0, 10, 15, 20, and 30 min). Then, 10 mL of a  $\text{Y}(\text{NO}_3)_3$  solution was added. Second, the whole solution was transferred into a 100 mL Teflon-lined stainless steel autoclave (HeNan JingHua Instrument Co., Ltd, Gongyi, China) with 50% of the volume filled and treated at different temperatures for different times. Finally, the as-synthesized sample was centrifuged and washed with deionized water several times to remove soluble salts and then dried at 60 °C for 12 h.

### 2.2. Characterization

The crystalline phases of the specimen were analyzed by an Empyrean X-ray diffractometer (PANalytical B.V., Almelo, the Netherlands) with  $\text{Cu K}\alpha$  radiation ( $\lambda = 0.154056$  nm) at a scanning rate of 0.05 deg/s from 10° to 80°. The morphology of the crystals and the particle size were investigated by the ZEISS SUPRA 55 field-emission scanning electron microscope (Carl Zeiss NTS GmbH, Aalen, Germany). The microstructure was characterized by TEM and high-resolution transmission electron microscopy (HRTEM; JEOL 2100F, JEOL Co., Ltd., Tokyo, Japan). Emission and excitation spectra curves were recorded on the F-7000 FL spectrophotometer (HITACHI, Tokyo, Japan). The optical absorption spectra were recorded at a wavelength range of 200–1000 nm by the UV–VIS U-3900 spectrophotometer (HITACHI, Tokyo, Japan).

## 3. Results and Discussion

### 3.1. Effects of Oxidation Time

To study the effect of oxidation time, the colors of the precursor solution in the air for different times were observed, as shown in Figure 1. As the stirring time increased, the color of the precursor solution gradually became darker. This indicated that low-valence manganese ions were gradually oxidized to high-valence manganese by oxygen.

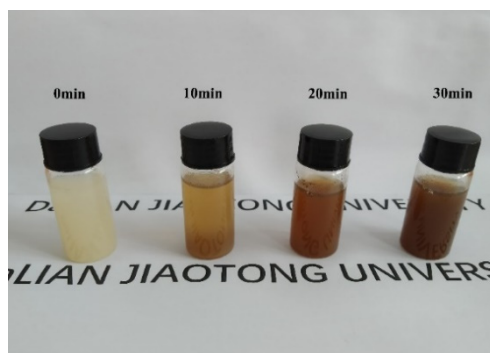


**Figure 1.** Digital images of the precursor solution with different stirring times.

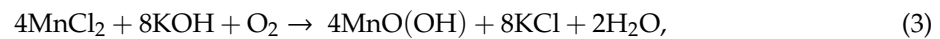
Figure 2 shows the XRD patterns of hydrothermal products obtained at 180 °C for 24 h after oxidation at different times in the air. Characteristic peaks of  $Y(OH)_3$ ,  $MnO(OH)$ , and  $MnO(OH)_2 \cdot H_2O$  can be seen in Figure 2a. The appearance of high-valence manganese is due to the presence of the air in a confined space during the hydrothermal treatment and also drying in the air. The oxygen present can act as an oxidant, as shown in the following reaction equation [23–26]:



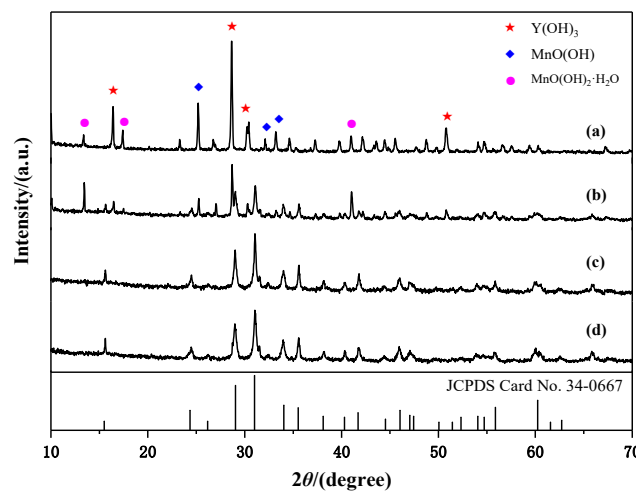
$YMn_2O_5$  in the product was detected, when the stirring time was 10 min, as shown in Figure 2b. Under alkaline conditions,  $MnCl_2$  reacted with the alkali to form the  $Mn(OH)_2$  precursor. The reaction equation was as follows:



$Mn^{2+}$  ion and  $Mn(OH)_2$  were partially or completely oxidized to manganese with a high valence state. The oxidation reaction was favored by increased alkalinity:

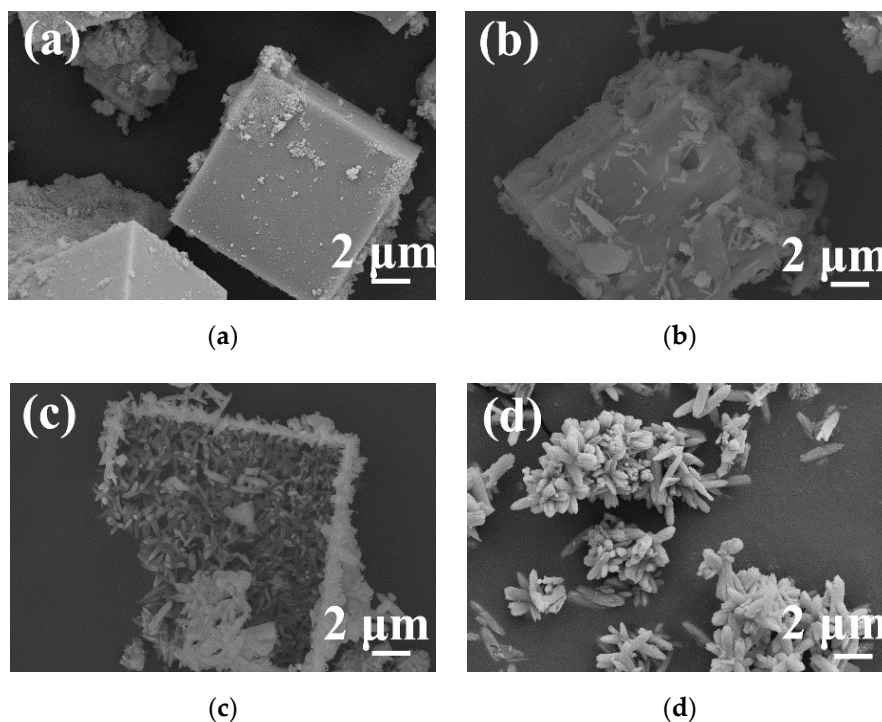


When the stirring time increased to 20 min, diffraction peaks from impurity phases disappeared. The main diffraction peaks corresponded to  $YMn_2O_5$  (JCPDS Card No. 34-0667). It can be observed that the intensities of the peaks did not change as the stirring time increased.



**Figure 2.** XRD patterns of products obtained by hydrothermal treatment at 180 °C at different oxidation times in the air: (a) 0 min; (b) 10 min; (c) 20 min; (d) 30 min.

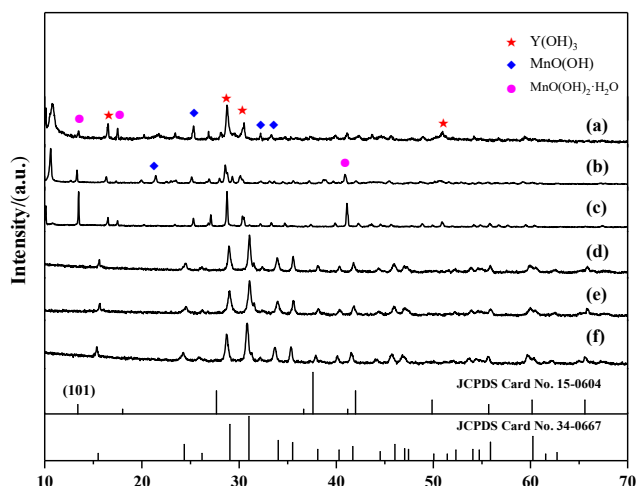
Figure 3 shows the SEM images of hydrothermal products obtained at 180 °C for 24 h after different stirring times. As shown in Figure 3a, when the stirring time was very short, the obtained sample had a solid cubic shape. When the stirring time was 10 min (Figure 3b), the sample underwent a dissolution process, which was indicated by the presence of pores on the surface. When the stirring time was 20 min, a large number of nanoparticles developed into nanorods with an approximately uniform size, as shown in Figure 3c. Upon prolonging the stirring time to 30 min (Figure 3d), the sample became a spindle-like rod that exhibited flower-like aggregates.



**Figure 3.** SEM images of hydrothermal products obtained with different stirring times: (a) 0 min; (b) 10 min; (c) 20 min; (d) 30 min.

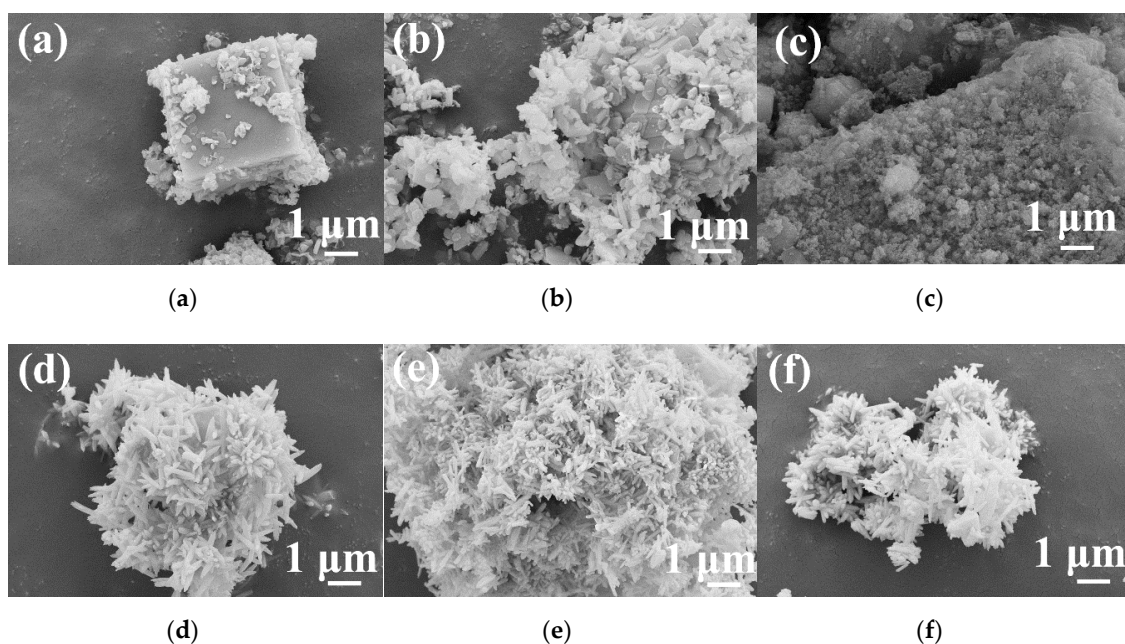
### 3.2. Effects of Hydrothermal Conditions

To ascertain the effect of the hydrothermal temperature on the products, hydrothermal synthesis experiments were carried out at six different temperatures for 24 h after stirring for 30 min in the air. The as-prepared samples were analyzed with XRD, as shown in Figure 4. When the hydrothermal temperature increased from 140 to 170 °C, the product was confirmed to be a mixture of  $Y(OH)_3$ ,  $MnO(OH)$ , and  $MnO(OH)_2 \cdot H_2O$  phases, of which the intensity gradually increased, as shown in Figure 4a–c. The crystallite sizes were calculated using the Scherrer equation, i.e.,  $D = K\lambda/B\cos\theta$ . The calculated average crystallite sizes of the (101) crystal plane were 64.5, 77.9, and 87.6 nm, respectively. It was revealed that synthesis temperatures of 170 °C and below were beneficial to the formation of  $MnO(OH)_2 \cdot H_2O$ . When the hydrothermal temperature increased to 180 °C, the XRD results indicated that single-phase  $YMn_2O_5$  (JCPDS Card No. 34-0667) was formed successfully, as shown in Figure 4e. The characteristic peaks at  $2\theta = 15.5^\circ, 24.36^\circ, 29.06^\circ, 31.02^\circ, 34.03^\circ, 35.52^\circ,$  and  $60.24^\circ$  can be assigned to the corresponding (001), (200), (201), (211), (102), and (112) planes, respectively. No peaks from any other phases were detected, which indicated that the product obtained in the present synthesis condition was highly pure. With the increasing hydrothermal temperature, the XRD diffraction peaks appeared to exhibit no obvious changes, indicating that increasing the temperature further had no effect on the structure of the obtained products. To our knowledge, the formation of the products should overcome the reaction barrier, which can usually be solved by raising the reaction temperature. As mentioned above, the lowest temperature for the synthesis of  $YMn_2O_5$  crystallites was 180 °C. Compared with that in Reference [21], the minimum synthesis temperature was reduced by 10 degrees.



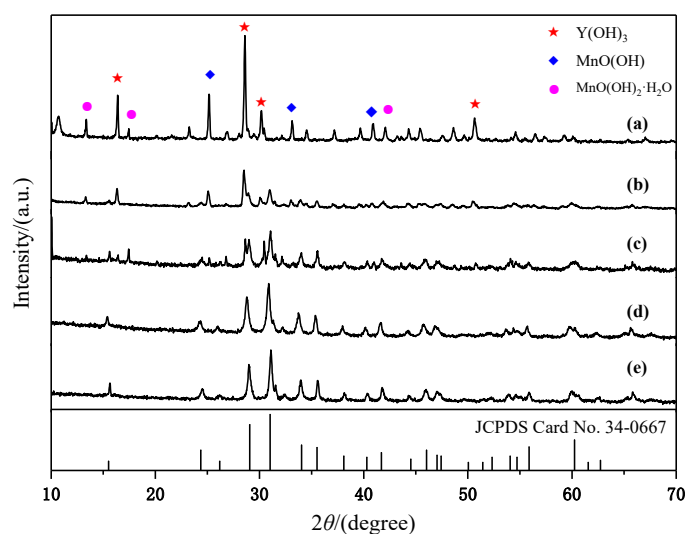
**Figure 4.** XRD patterns of samples synthesized at different hydrothermal temperatures: (a) 140 °C; (b) 160 °C; (c) 170 °C; (d) 180 °C; (e) 200 °C; (f) 220 °C.

Figure 5 displays the SEM images of samples prepared at different hydrothermal temperatures for 24 h after stirring for 30 min in the air. The morphology of the sample at 140 °C was regular microcubes with irregular flake-like particles attached to the surface, as presented in Figure 5a. When the hydrothermal temperature increased to 160 and 170 °C, more flake-like particles appeared around irregular microcubes, as shown in Figure 5b,c. When the hydrothermal temperature reached 180 °C, the observed aggregates were composed of micro-sized rod-like particles, as shown in Figure 5d. Upon elevating the hydrothermal temperature further, there was no apparent change in the morphology. According to Figures 4 and 5, these SEM images demonstrated that the morphology of the samples was related to the crystalline phase of the particles. Obviously, the MnO(OH) and MnO(OH)<sub>2</sub>·H<sub>2</sub>O particles assumed a flake-like shape, and the Y(OH)<sub>3</sub> particles had a cube-like shape, while the YMn<sub>2</sub>O<sub>5</sub> nanoparticles took on a rod-like shape.



**Figure 5.** SEM images of samples synthesized at different hydrothermal temperatures: (a) 140 °C; (b) 160 °C; (c) 170 °C; (d) 180 °C; (e) 200 °C; (f) 220 °C.

Different hydrothermal times were investigated to validate the impact of this parameter. The XRD patterns were obtained after hydrothermal treatments at 180 °C for different times, as shown in Figure 6. When the hydrothermal time was 6 h, MnO(OH), MnO(OH)<sub>2</sub>·H<sub>2</sub>O, and Y(OH)<sub>3</sub> appeared in the hydrothermal sample. After 12 h, two new diffraction peaks appeared at 2θ values of approximately 29.3° and 30.9°, which coincided with the peaks in JCPDS Card No. 34-0667. This indicated that the YMn<sub>2</sub>O<sub>5</sub> phase started to form or develop. After 18 h, the intensity of the impurity phase diffraction peaks decreased, while the intensity of the YMn<sub>2</sub>O<sub>5</sub> peaks increased. After 24 h, the impurity peaks disappeared entirely, and only the diffraction peak from YMn<sub>2</sub>O<sub>5</sub> remained. At this point, the hydrothermal sample comprised a pure YMn<sub>2</sub>O<sub>5</sub> powder. There was no apparent effect on the phase structure, after the hydrothermal time increased to 48 h.



**Figure 6.** XRD patterns of samples synthesized at 180 °C for different hydrothermal times: (a) 6 h; (b) 12 h; (c) 18 h; (d) 24 h; (e) 48 h.

The morphological evolution provides an understanding of the formation process of YMn<sub>2</sub>O<sub>5</sub> crystals. For this purpose, samples with different hydrothermal times were observed with SEM, as shown in Figure 7. When the hydrothermal time was 6 h, the sample contained cube-like shapes that were covered with flake-like particles. After 12 h, the cube structure began to dissolve, and there were pits and pores that appeared on the surface of the cubes. A small amount of YMn<sub>2</sub>O<sub>5</sub> seeds formed at this time. When the hydrothermal time increased to 18 h, the flake-like particles disappeared, and rod-like structures appeared. When the hydrothermal time reached 24 h, part of the product morphology appeared spindle-like. Due to the elongation of the holding time, the nucleation position and growth direction of the YMn<sub>2</sub>O<sub>5</sub> particles had a preferred orientation, which led to the formation of the morphology. When the hydrothermal time extended to 48 h, there was almost no change in the morphology of the product, which is consistent with the results shown in Figure 6.

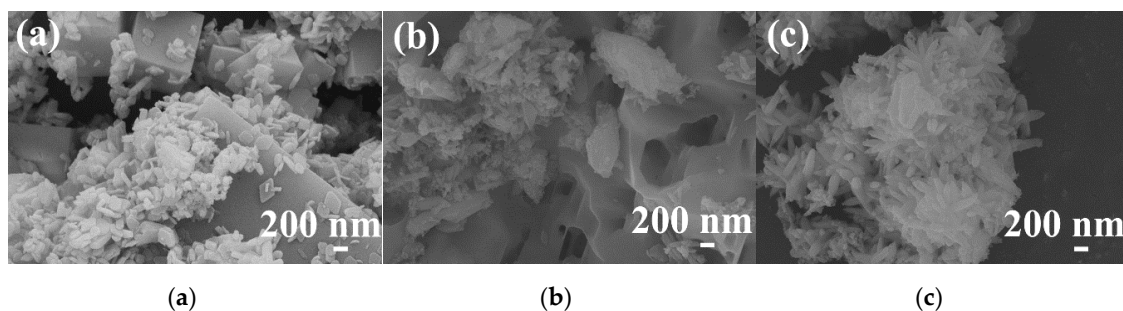


**Figure 7.** Cont.

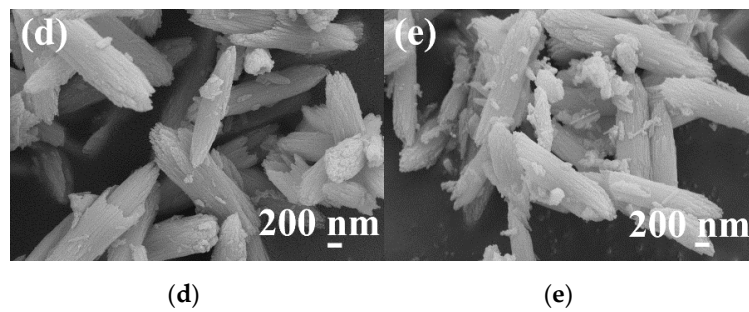


**Figure 7.** SEM images of samples synthesized at different hydrothermal times: (a) 6 h; (b) 12 h; (c) 18 h; (d) 24 h; (e) 48 h.

To obtain additional information about the  $\text{YMn}_2\text{O}_5$  powder, TEM, HRTEM, and selected area electron diffraction (SAED) analyses were performed, and the results are shown in Figure 8. Figure 8a further demonstrates that the  $\text{YMn}_2\text{O}_5$  product consisted of a uniform rod-like powder with a diameter range of 50–70 nm. The HRTEM image (Figure 8b,c) clearly shows lattice fringes with an interplanar spacing of 0.57 nm, which is attributed to the (001) plane. Figure 8d shows the SAED pattern of individual nanorods, and the result suggested that the individual  $\text{YMn}_2\text{O}_5$  nanorods were single crystals. According to the above analysis, the growth direction of the  $\text{YMn}_2\text{O}_5$  nanorods was along the [001] direction.

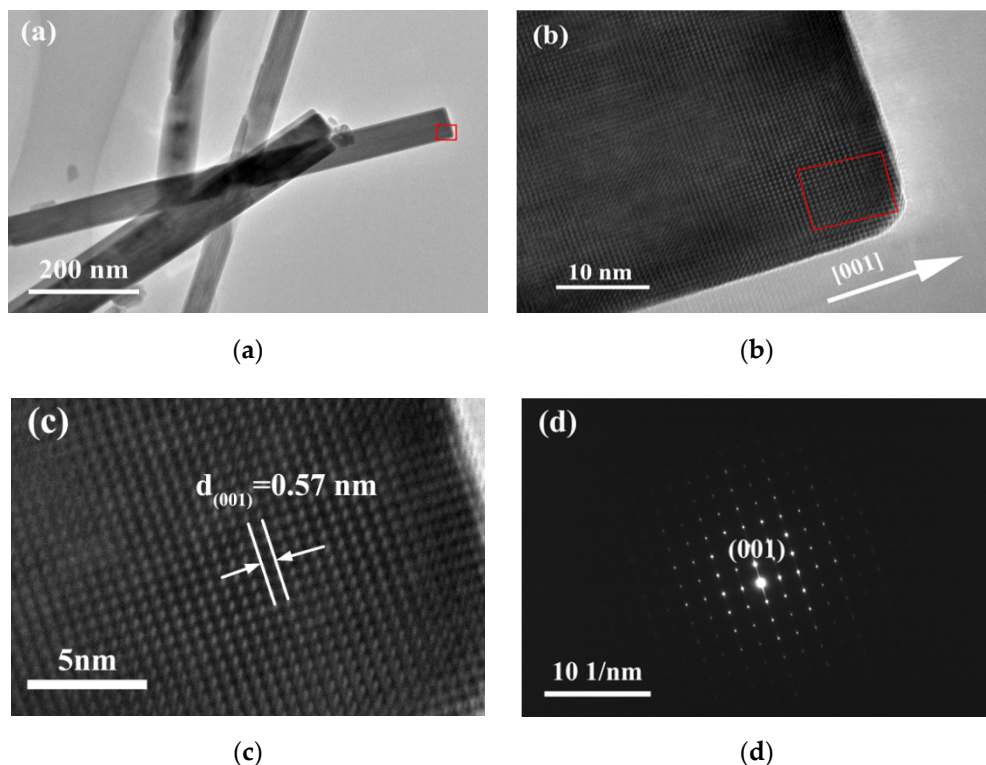


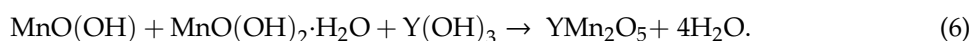
**Figure 8.** TEM, high-resolution transmission electron microscopy (HRTEM), and selected area electron diffraction (SAED) images of  $\text{YMn}_2\text{O}_5$ : (a) TEM; (b) HRTEM; (c) amplification of the HRTEM; (d) SAED.

### 3.3. Mechanism Analysis

Based on the above discussion, the formation process and growth mechanism of  $\text{YMn}_2\text{O}_5$  were speculated as following:



Before the hydrothermal reaction, KOH solids were added to the  $\text{MnCl}_2$  solution to obtain  $\text{Mn}(\text{OH})_2$ , which can be oxidized into  $\text{MnO}(\text{OH})$  and  $\text{MnO}(\text{OH})_2 \cdot \text{H}_2\text{O}$  brown precipitates in the air by oxygen [27]. After adding the  $\text{Y}(\text{NO}_3)_3$  solution, a gel was obtained. The precursor solution contained  $\text{Y}^{3+}$ ,  $\text{Mn}^{3+}$ ,  $\text{Mn}^{4+}$ , and other ions. When the mixture was transferred into the autoclave, the precursor transformed into  $\text{Y}(\text{OH})_x^{3-x}$  and  $\text{Mn}(\text{OH})_y^{2x-y}$  ion clusters at high temperature and high pressure [28]. As the temperature increased and the time increased,  $\text{YMn}_2\text{O}_5$  compounds were formed continuously by satisfying thermodynamic requirements. Combined with the previously mentioned reaction Equations (1)–(4), the reaction equation was as follows:



According to the classical crystal growth theory, the growth of  $\text{YMn}_2\text{O}_5$  crystals synthesized by the hydrothermal synthesis method can be divided into the following stages. The first is the dissolution stage. Under alkaline conditions, a mixture composed of  $\text{MnO}(\text{OH})$ ,  $\text{MnO}(\text{OH})_2 \cdot \text{H}_2\text{O}$ , and  $\text{Y}(\text{OH})_3$  was observed at room temperature. In hydrothermal conditions, precursors were dissolved at high temperature and high pressure and entered into the mixed aqueous solution in the form of Y, Mn ions or ionic groups. Second, there was a thermal convection and concentration difference between the dissolving zone and the growth zone. These ions or clusters reached critical nucleation concentrations that were transported to the growth zone for nucleation. After that, these ions or groups of ions were adsorbed, decomposed, and desorbed at the growth interface, and the adsorbed material moved at the interface. The final step is crystallization [29].

The growth mechanism of  $\text{YMn}_2\text{O}_5$  is due to a dissolution–recrystallization mechanism. The schematic in Figure 9 illustrates the process for  $\text{YMn}_2\text{O}_5$  crystals. The insoluble precursors were obtained at room temperature. During the hydrothermal reaction, the precursors, which did not dissolve readily at room temperature, began to dissolve. The ions were attached to the surface of the precursor, which inhibited the over-dissolution of the precursor. As the concentration of ions increased, the precursor solution reached a critical nucleation threshold, and  $\text{YMn}_2\text{O}_5$  was obtained by homogeneous nucleation and growth on the surface of the precursor. As the reaction proceeded, the concentration in the system decreased, which promoted the dissolution of the precursor and provided the growth unit for the crystal nucleus. The preferred growth orientation of  $\text{YMn}_2\text{O}_5$  is anisotropic in nature [21,30]. Finally, the growth direction of the crystallized  $\text{YMn}_2\text{O}_5$  was along the crystallography  $c$  axis and parallel to the  $[001]$  direction.

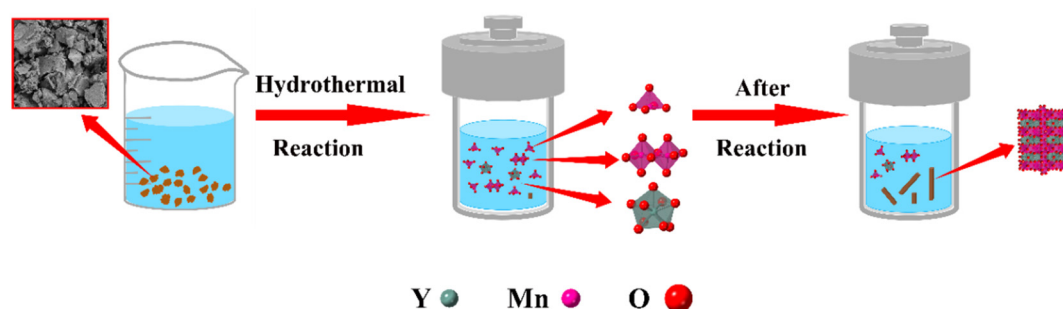
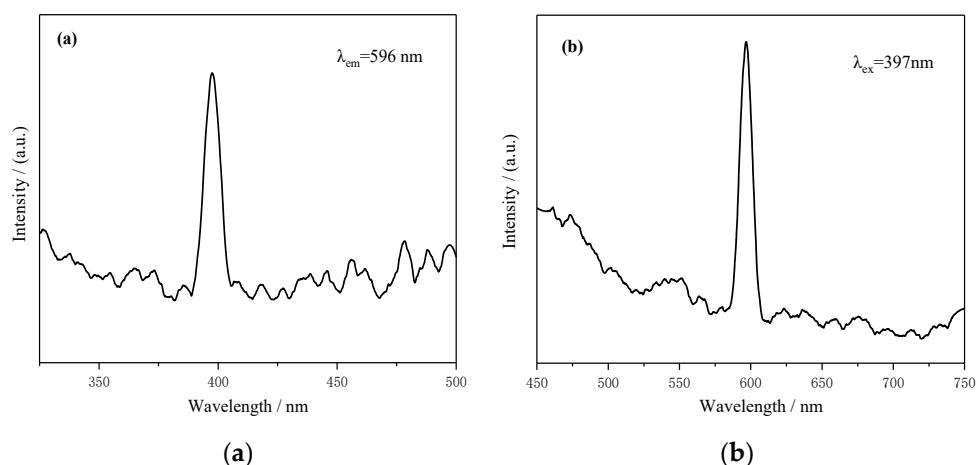


Figure 9. Schematic model of dissolution and recrystallization for  $\text{YMn}_2\text{O}_5$ .

It is well-known that the product can be influenced by the reaction temperature, time, and concentration. In this work, we paid special attention to the influence of oxygen. Oxygen as an oxidant transformed  $\text{Mn}^{2+}$  ions into  $\text{Mn}^{3+}$  and  $\text{Mn}^{4+}$  ions. The oxidation time is a very critical factor and can affect the balance of manganese ion concentrations in the solution. In addition, sufficient reaction temperature and time should be used to overcome the reaction barrier.

### 3.4. Luminescent Properties

To investigate the luminescence characteristics of the samples, the excitation and emission spectra were measured and are shown in Figure 10. The sample was prepared at 180 °C for 24 h after stirring for 30 min in the air. All the excitation spectra monitored at 596 nm (see Figure 10a) were composed of a group of sharp lines in the range of 350–500 nm. The strongest excitation peak was located at 397 nm. With the excitation of 397 nm radiation, it can be seen that an intense emission peak was located at 596 nm, as shown in Figure 10b. As well-known,  $Mn^{4+}$  ions are in the octahedral crystal field, and orange emission occurs under excitation conditions, which is due to the  ${}^2E_g \rightarrow {}^4A_{2g}$  transition of the 3d orbital energy levels [22]. Due to the Jahn–Teller effect in  $YMn_2O_5$  crystals, the lattice distortion of  $MnO_6$  octahedron caused the blueshift of the Mn emission wavelength [31].



**Figure 10.** Excitation spectra (a) and emission spectra (b) of the  $YMn_2O_5$  sample.

Figure 11a shows the absorption spectra of the  $YMn_2O_5$  sample. An absorbance also occurred close to 900 nm, suggesting that the sample can be effectively absorbed in the visible light range. According to the Kubelka–Munk (K–M) theory [32], the indirect bandgap of the  $YMn_2O_5$  sample can be estimated from the plot of  $(\alpha hv)^{1/2}$  versus  $hv$ , as shown in Figure 11b, where  $\alpha$  is the K–M absorption coefficient and  $hv$  is the incident photon energy. The linear portion of the plot was extrapolated to the axis of the abscissa to yield the energy bandgap. The obtained energy bandgap of the resulted samples was 1.18 eV, which is consistent with Reference [14].

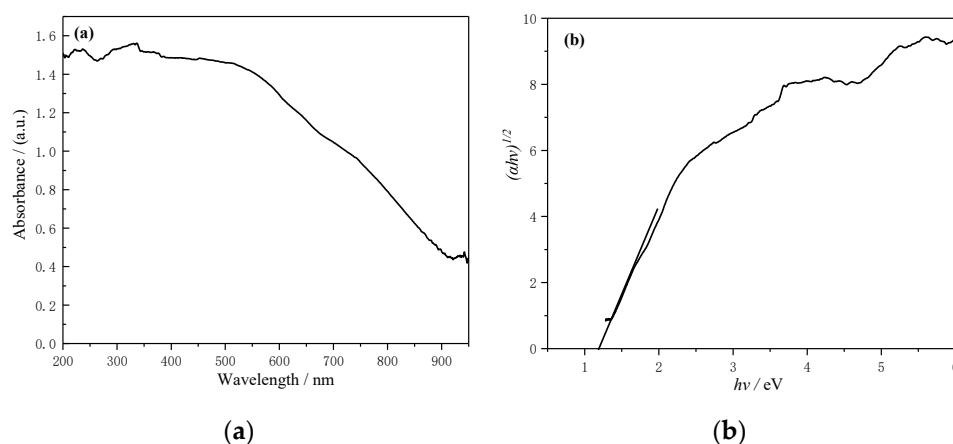


**Figure 11.** (a) UV–VIS absorption spectra of the  $YMn_2O_5$  sample, (b) Tauc–Mott plot of  $(\alpha hv)^{1/2}$  versus  $hv$ .

#### 4. Conclusions

A hydrothermal method was employed to fabricate  $\text{YMn}_2\text{O}_5$  with oxygen as an oxidant. The conditions of the hydrothermal reaction temperature and time, stirring time, and luminescent properties are analyzed and discussed in detail herein.

It was demonstrated that a single-crystal nanorod-like  $\text{YMn}_2\text{O}_5$  powder with a uniform size could be obtained by oxidizing the material for 30 min in the air and treating it hydrothermally at 180 °C for 24 h. Full oxidation in the air can change manganese ions from divalent to trivalent and tetravalent. Moreover, the hydrothermal temperature and time are the key factors for determining the nucleation and growth of  $\text{YMn}_2\text{O}_5$ . The growth direction of the nanorods was along the crystallography *c* axis and parallel to the [001] direction. The growth mechanism of  $\text{YMn}_2\text{O}_5$  followed a dissolution–crystallization mechanism. Under the 397 nm excitation, the  $\text{Mn}^{4+}$  ions exhibited an intense orange emission at 596 nm. The  $\text{YMn}_2\text{O}_5$  powder has potential applications in optoelectronic areas. The energy bandgap of  $\text{YMn}_2\text{O}_5$  powders was 1.18 eV.

**Author Contributions:** Data curation, Y.L. and Z.S.; Writing—original draft, J.S. and H.H.; Writing—review & editing, J.W. All authors have read and agreed to the published version of the manuscript.

**Funding:** This work was supported by the National Key Research and Development Program of China (2017YFB0310300) and Natural Foundation of Liaoning Province (2019-ZD-0090).

**Conflicts of Interest:** The authors declare no conflict of interest.

#### References

1. Schmid, H. Multi-ferroic magnetoelectrics. *Ferroelectrics* **1994**, *162*, 317–338. [[CrossRef](#)]
2. Huang, Z.J.; Cao, Y.; Sun, Y.Y.; Xue, Y.Y.; Chu, C.W. Coupling between the ferroelectric and antiferromagnetic orders in  $\text{YMnO}_3$ . *Phys. Rev. B* **1997**, *56*, 2623–2626. [[CrossRef](#)]
3. Fiebig, M.; Lottermoser, T.; Frohlich, D.; Goltsev, A.V.; Pisarev, R.V. Observation of coupled magnetic and electric domains. *Nature* **2002**, *419*, 818–820. [[CrossRef](#)] [[PubMed](#)]
4. Lorenz, B.; Litvinchuk, A.P.; Gospodinov, M.M.; Chu, C.W. Field-induced reentrant novel phase and a ferroelectric-magnetic order coupling in  $\text{HoMnO}_3$ . *Phys. Rev. Lett.* **2004**, *92*, 087204. [[CrossRef](#)] [[PubMed](#)]
5. Hur, N.; Park, S.; Sharma, P.A.; Ahn, J.S.; Guha, S.; Cheong, S.W. Electric polarization reversal and memory in a multiferroic material induced by magnetic fields. *Nature* **2004**, *429*, 392–395. [[CrossRef](#)] [[PubMed](#)]
6. Alonso, J.A.; Casais, M.T.; MartinezLope, M.J.; Rasines, I. High oxygen pressure preparation, structural refinement, and thermal behavior of  $\text{RMn}_2\text{O}_5$  ( $\text{R} = \text{La, Pr, Nd, Sm, Eu}$ ). *J. Solid State Chem.* **1997**, *129*, 105–112. [[CrossRef](#)]
7. Chapon, L.C.; Blake, G.R.; Gutmann, M.J.; Park, S.; Hur, N.; Radaelli, P.G.; Cheong, S.W. Structural anomalies and multiferroic behavior in magnetically frustrated  $\text{TbMn}_2\text{O}_5$ . *Phys. Rev. Lett.* **2004**, *93*, 177402. [[CrossRef](#)]
8. Inomata, A.; Kohn, K. Pyroelectric effect and possible ferroelectric transition of helimagnetic  $\text{GdMn}_2\text{O}_5$ ,  $\text{TbMn}_2\text{O}_5$  and  $\text{YMn}_2\text{O}_5$ . *J. Phys.: Condens. Matter* **1996**, *8*, 2673–2678. [[CrossRef](#)]
9. Kobayashi, S.; Osawa, T.; Kimura, H.; Noda, Y.; Kagomiya, I.; Kohn, K. Reinvestigation of simultaneous magnetic and ferroelectric phase transitions in  $\text{YMn}_2\text{O}_5$ . *J. Phys. Soc. Jpn.* **2004**, *73*, 1593–1596. [[CrossRef](#)]
10. Noda, Y.; Kimura, H.; Fukunaga, M.; Kobayashi, S.; Kagomiya, I.; Kohn, K. Magnetic and ferroelectric properties of multiferroic  $\text{RMn}_2\text{O}_5$ . *J. Phys. Condens. Matter* **2008**, *20*, 434206. [[CrossRef](#)]
11. Kagomiya, I.; Kakimoto, K.; Ohsato, H. Precursor phenomenon on ferroelectric transition in multiferroic  $\text{YMn}_2\text{O}_5$ . *J. Eur. Ceram. Soc.* **2010**, *30*, 255–258. [[CrossRef](#)]
12. Ma, C.; Yan, J.Q.; Dennis, K.W.; McCallum, R.W.; Tan, X. Size-dependent magnetic properties of high oxygen content  $\text{YMn}_2\text{O}_5$   $\pm \delta$  multiferroic nanoparticles. *J. Appl. Phys.* **2009**, *105*, 033908. [[CrossRef](#)]
13. De la Calle, C.; Alonso, J.A.; Martinez-Lope, M.J.; Garcia-Hernandez, M.; Andre, G. Synthesis under high-oxygen pressure, magnetic and structural characterization from neutron powder diffraction data of  $\text{YGa}_{1-x}\text{Mn}_{1+x}\text{O}_5$  ( $x = 0.23$ ): A comparison with  $\text{YMn}_2\text{O}_5$ . *Mater. Res. Bull.* **2008**, *43*, 197–206. [[CrossRef](#)]
14. Yang, H.; Wang, S.F.; Xian, T.; Wei, Z.Q.; Feng, W.J. Fabrication and photocatalytic activity of  $\text{YMn}_2\text{O}_5$  nanoparticles. *Mater. Lett.* **2011**, *65*, 884–886. [[CrossRef](#)]

15. Wang, S.; Zhang, C.; Sun, G.; Chen, B.; Xiang, X.; Ding, Q.; Zu, X. Chelating agents role on phase formation and surface morphology of single orthorhombic  $\text{YMn}_2\text{O}_5$  nanorods via modified polyacrylamide gel route. *Sci. China Chem.* **2014**, *57*, 402–408. [[CrossRef](#)]
16. Li, S.H.; Lei, G.P.; Peng, H. Synthesized and magnetic and ferroelectric phase transitions of single phase multiferroic  $\text{YMn}_2\text{O}_5$  nanoparticles through microwave assisted polyacrylamide gel method. *Ferroelectrics* **2017**, *520*, 135–143. [[CrossRef](#)]
17. Wang, S.F.; Yang, H.; Xian, T.; Wei, Z.Q.; Ma, J.Y.; Feng, W.J. Nano  $\text{YMn}_2\text{O}_5$  Visible-light-driven Semiconductor Photocatalyst. *J. Inorg. Mater.* **2011**, *26*, 1164–1168. [[CrossRef](#)]
18. Gao, Y.; Wu, Y.J.; Chen, X.M.; Cheng, J.P.; Lin, Y.Q.; Ma, Y. Dense  $\text{YMn}_2\text{O}_5$  Ceramics Prepared by Spark Plasma Sintering. *J. Am. Ceram. Soc.* **2008**, *91*, 3728–3730. [[CrossRef](#)]
19. Zhang, T.; Li, H.; Yang, Z.; Cao, F.R.; Li, L.; Chen, H.J.; Liu, H.; Xiong, K.; Wu, J.; Hong, Z.L.; et al. Electrospun  $\text{YMn}_2\text{O}_5$  nanofibers: A highly catalytic activity for NO oxidation. *Appl. Catal. B* **2019**, *247*, 133–141. [[CrossRef](#)]
20. Li, L.L.; Wu, S.Y.; Chen, X.M. Multiferroic  $\text{YMn}_2\text{O}_5$  fine powders derived from hydrothermal process. *J. Mater. Sci. Mater. Electron.* **2009**, *20*, 1159–1163. [[CrossRef](#)]
21. Mei, Y.X.; Wu, S.P. Morphology control of  $\text{YMn}_2\text{O}_5$  nanocrystals by hydrothermal synthesis and their magnetic properties. *RSC Adv.* **2013**, *3*, 11888–11894. [[CrossRef](#)]
22. Zhou, Z.; Zhou, N.; Xia, M.; Yokoyama, M.; Hintzen, H.T. Research progress and application prospects of transition metal  $\text{Mn}^{4+}$ -activated luminescent materials. *J. Mater. Chem. C* **2016**, *4*, 9143–9161. [[CrossRef](#)]
23. Hu, C.C.; Wu, Y.T.; Chang, K.H. Low-temperature hydrothermal synthesis of  $\text{Mn}_3\text{O}_4$  and  $\text{MnOOH}$  single crystals: Determinant influence of oxidants. *Chem. Mater.* **2008**, *20*, 2890–2894. [[CrossRef](#)]
24. Zheng, W.J.; Pang, W.Q.; Meng, G.Y.; Peng, D.K. Hydrothermal synthesis and characterization of  $\text{LaCrO}_3$ . *J. Mater. Chem.* **1999**, *9*, 2833–2836. [[CrossRef](#)]
25. Jana, S.; Basu, S.; Pande, S.; Ghosh, S.K.; Pal, T. Shape-selective synthesis, magnetic properties, and catalytic activity of single crystalline  $\beta$ - $\text{MnO}_2$  nanoparticles. *J. Phys. Chem. C* **2007**, *111*, 16272–16277. [[CrossRef](#)]
26. Li, F.; Wu, J.; Qin, Q.; Li, Z.; Huang, X. Facile synthesis of  $\gamma$ - $\text{MnOOH}$  micro/nanorods and their conversion to  $\beta$ - $\text{MnO}_2$ ,  $\text{Mn}_3\text{O}_4$ . *J. Alloys Compd.* **2010**, *492*, 339–346. [[CrossRef](#)]
27. Cha, D.K.; Park, S.M. Electrochemical oxidation of  $\text{Mn}(\text{OH})_2$  in alkaline media. *J. Electrochem. Soc.* **1997**, *144*, 2573–2580. [[CrossRef](#)]
28. Vedmid, L.B.; Yankin, A.M.; Fedorova, O.M.; Balakirev, V.F. Evolution of phase equilibrium states in the Y-Mn-O system in the thermal dissociation of the compound  $\text{YMn}_2\text{O}_5$ . *Russ. J. Inorg. Chem.* **2014**, *59*, 519–523. [[CrossRef](#)]
29. Wu, Y.H. *An Introduction to Nanomaterials*; Chemical Industry Press: Beijing, China, 2009.
30. Jun, Y.W.; Choi, J.S.; Cheon, J. Shape control of semiconductor and metal oxide nanocrystals through nonhydrolytic colloidal routes. *Angew. Chem. Int. Ed.* **2006**, *45*, 3414–3439. [[CrossRef](#)]
31. Shang, M.M.; Li, C.X.; Lin, J. How to produce white light in a single-phase host? *Chem. Soc. Rev.* **2014**, *43*, 1372–1386. [[CrossRef](#)]
32. Yang, L.; Kruse, B. Revised Kubelka-Munk theory. I. Theory and application. *J. Opt. Soc. Am. A* **2004**, *21*, 1933–1941. [[CrossRef](#)] [[PubMed](#)]

